Usefulness of [18F]-DA and [18F]-DOPA for PET imaging in a mouse model of pheochromocytoma

Lucia Martiniova[a,j], **Susannah Cleary**[b], **Edwin W. Lai**[a], **Dale O. Kiesewetter**[c], **Jurgen Seidel**[d], **Linda F. Dawson**[e], **Jacqueline K. Phillips**[e,f], **David Thomasson**[g], **Xiaoyuan Chen**[c], **Graeme Eisenhofer**[h], **James F. Powers**[i], **Richard Kvetnansky**[j], and **Karel Pacak**[a,*]

[a]Program in Reproductive and Adult Endocrinology, Eunice Kennedy Shriver National Institute of Child Health and Human Development, NIH, Bethesda, MD 20892, USA

[b]Clinical Neurocardiology Section, National Institute of Neurological Disorders and Stroke, NIH, Bethesda, MD 20892, USA

[c]Laboratory for Molecular Imaging and Nanomedicine, National Institute of Biomedical Imaging and Bioengineering, NIH, Bethesda, MD 20892, USA

[d]Molecular Imaging Program, National Cancer Institute, NIH, Bethesda, MD 20892, USA

[e]Faculty of Health Sciences, Murdoch University, South St. Murdoch, Perth, WA 6150, Australia

[f]Australian School of Advanced Medicine, Macquarie University, Sydney, NSW 2109, Australia

[g]Laboratory of Diagnostic Radiology, Warren Grant Magnuson Clinical Center, National Institutes of Health, Bethesda, MD 20892, USA

[h]Institute of Clinical Chemistry and Laboratory Medicine and the Department of Medicine, University of Dresden, Dresden, 01307 Germany

[i]Department of Pathology, Tufts Medical Center, Boston, MA 02111, USA

[j]Institute of Experimental Endocrinology, Slovak Academy of Sciences, Bratislava, 83306 Slovakia

Abstract

Purpose—To evaluate the usefulness of [18F]-6-fluorodopamine ([18F]-DA) and [18F]-L-6-fluoro-3,4-dihydroxyphenylalanine ([18F]-DOPA) positron emission tomography (PET) in the detection of subcutaneous (s.c.) and metastatic pheochromocytoma in mice; to assess the expression of the norepinephrine transporter (NET) and vesicular monoamine transporters 1 and 2 (VMAT1 and VMAT2), all important for [18F]-DA and [18F]-DOPA uptake. Furthermore, to compare tumor detection by micro-computed tomography (microCT) to magnetic resonance imaging (MRI) in individual mouse.

Methods—SUV_{max} values were calculated from [18F]-DA and [18F]-DOPA PET, tumor-to-liver ratios (TLR) were obtained and expression of NET, VMAT1 and VMAT2 was evaluated.

*Corresponding author. NICHD, NIH, 10 Center Drive MSC-1109, Bethesda, MD, 20892-1109 USA. Tel.: +1 301 402 4594; fax: +1 301 402 4712. karel@mail.nih.gov. .

Results—[^{18}F]-DA detected less metastatic lesions compared to [^{18}F]-DOPA. TLR values for liver metastases were 2.26–2.71 for [^{18}F]-DOPA and 1.83–2.83 for [^{18}F]-DA. A limited uptake of [^{18}F]-DA was found in s.c. tumors (TLR=0.22-0.27) compared to [^{18}F]-DOPA (TLR=1.56-2.24). Overall, NET and VMAT2 were expressed in all organ and s.c. tumors. However, s.c. tumors lacked expression of VMAT1. We confirmed [^{18}F]-DA's high affinity for the NET for its uptake and VMAT1 and VMAT2 for its storage and retention in pheochromocytoma cell vesicles. In contrast, [^{18}F]-DOPA was found to utilize only VMAT2.

Conclusion—MRI was superior in the detection of all organ tumors compared to microCT and PET. [^{18}F]-DOPA had overall better sensitivity than [^{18}F]-DA for the detection of metastases. Subcutaneous tumors were localized only with [^{18}F]-DOPA, a finding that may reflect differences in expression of VMAT1 and VMAT2, perhaps similar to some patients with pheochromocytoma where [^{18}F]-DOPA provides better visualization of lesions than [^{18}F]-DA.

1. Introduction

In clinical practice, various imaging techniques are used to localize pheochromocytoma, a rare neuroendocrine tumor arising from chromaffin cells [1]. These tumors are characterized by the synthesis, storage, metabolism and release of catecholamines [2]. Even though metastatic pheochromocytoma is generally slow growing, the prognosis of patients with disseminated disease is often poor, with a 5-year survival rate of usually less than 50% [3,4]. This is due to the fact that, currently, there is no effective chemotherapeutic regimen [5]. Therefore, the development of animal models for testing new imaging methods and probes to visualize and monitor tumor growth, as well as other tumor characteristics, is crucial for new drug development.

In recent years, positron emission tomography (PET) has rapidly become a valuable diagnostic tool in the study of pheochromocytomas, particularly with the development of new targeted PET radiopharmaceuticals such as [^{18}F]-6-fluorodopamine ([^{18}F]-DA) [6,7] and [^{18}F]-$_L$-6-fluoro-3,4-dihydroxyphenylalanine ([^{18}F]-DOPA) [8]. Functional imaging studies with [^{18}F]-DA and [^{18}F]-DOPA have the advantage over anatomical imaging of superior specificity for identification of pheochromocytomas [9,10]. Uptake of [^{18}F]-DA, a dopamine analogue, occurs via the cell membrane norepinephrine transporter (NET) [11]. Desipramine, a tricyclic anti-depressant, functions as an inhibitor of the uptake-1 mechanism involved in amine transport into cells [12] and has been used to evaluate the specificity of the NET transporter for [^{18}F]-DA uptake [13,14]. [^{18}F]-DOPA, an analogue of the dopamine precursor, DOPA, is incorporated into tumor cells via the aromatic amino acid transporter [15]. Upon entering the cells, [^{18}F]-DOPA is decarboxylated by the aromatic amino acid decarboxylase to [^{18}F]-DA and sequestered by vesicular monoamine transporters (VMAT1 and VMAT2) into catecholamine storage vesicles. The aromatic amino acid transporters, NET, VMAT1 and VMAT2 are specifically expressed in chromaffin cells and pheochromocytomas [16]. In this study, VMAT inhibitors, such as reserpine (VMAT1/

VMAT2 inhibitor) and tetrabenazine (VMAT2 inhibitor) [17], have been used to evaluate the importance of [18F]-DA and [18F]-DOPA uptake in mouse pheochromocytoma (MPC) cells.

Recently, we have described an animal model of metastatic pheochromocytoma and introduced [18F]-DA PET for the localization of liver lesions [18]. The aims of the present study were to compare the feasibility of a potentially more practical subcutaneous (s.c.) pheochromocytoma model against our previously established metastatic model, to evaluate [18F]-DOPA PET as an alternative modality for localization of lesions compared to micro-computed tomography (microCT) and magnetic resonance imaging (MRI) and to assess the importance of NET and VMATs in entry and storage of [18F]-DOPA and [18F]-DA in cells and tumors. These findings were aimed to determine whether these pheochromocytoma models are comparable to clinical imaging scenarios and, thus, appropriate for potential experiment drug treatments. The metastatic model involved diffuse spread of tumors after tail vein injection of MPC cells and the s.c. model represented by s.c. tumors after s.c. implantation of MPC cells.

2. Materials and methods

2.1. Cell culture and in vitro assays of [18F]-DA and [18F]-DOPA uptake and storage

MPC cells were kindly provided by Dr. A.S. Tischler [19] and were maintained in Dulbecco's Modified Minimum Essential Medium (GIBCO, Grand Island, NY, USA) supplemented with 10% (v/v) fetal calf serum, 5% fetal bovine serum and 1% (v/v) penicillin/streptomycin and maintained at 37°C and 5% CO_2.

To confirm the ability of MPC cells to incorporate [18F]-DA or [18F]-DOPA, in vitro radionuclide assays were conducted. MPC cells were seeded onto collagen-coated 12-well plates at a density of 2×10^5 cells per well and incubated for 24 h. At the commencement of uptake assays, cells were washed three times with phosphate-buffered saline (PBS, pH 7.4). Cells were then incubated for 30 min with the non-selective monoamine transporter antagonists: desipramine (1 μM, Sigma Chemical, St. Louis, MO, USA); tetrabenazine (10 μM, Sigma Chemical), an inhibitor of VMAT 2 [20,21] and reserpine (10 μM, Serpasil, Siba, Summit, NJ) an inhibitor of both VMAT1 and VMAT2 [22]. Uptake studies involved incubation of cells with 0.024 MBq/ml of [18F]-DA or 0.029 MBq/ml of [18F]-DOPA. Cells were harvested after incubation periods of either 10 (to assess "uptake") or 120 min (to assess "storage and retention").

At the termination of the radionuclide assays, cells were counted, and the radioactivity was measured on a Packard gamma counter (United Technologies). The uptake of [18F]-DA and [18F]-DOPA was described as counts per minute per number of cells per sample and expressed as "% normalized ratio of controls". The uptake was calculated by subtracting uptake in treated cells from control (untreated) cells. All experiments were performed in triplicate and repeated twice.

2.2. Animal model of pheochromocytoma

All animal studies were conducted in accordance with the principles and procedures outlined in the National Institutes of Health Guide for the Care and Use of Animals and approved by the Institutional Animal Care and Use Committee. Animals were housed in a pathogen-free facility under a 12-hour day/night cycle and had ad libitum access to food and water.

Our in vivo tumor model involved injections of MPC cells (suspended in 100 μl of sterile PBS) into two separate cohorts of 8–10 weeks old female athymic nude mice (NCr-nu, Taconic, Germantown, NY, USA). The first cohort of mice (n=9) received injection of 1×10^6 cells into the tail vein. A control group of mice (n=5) received intravenous injection of 100 μl PBS alone. The second cohort consisted of mice (n=4) that received s.c. injection of 5×10^6 cells. Mice were observed three times per week for evidence of distress, ascites, paralysis or excessive weight loss.

2.3. Anatomical imaging: microCT and MRI

Initial anatomical scans were conducted at 4 weeks post MPC implantation to determine the location and size of metastatic lesions. For both microCT and MRI, mice were anesthetized with isoflurane during scanning. For microCT, mice were imaged using a MicroCAT-II scanner (Siemens, Knoxville, TN, USA) [23]. The hepatobiliary contrast agent Fenestra Liver Contrast (LC) (Advanced Research Technologies) was injected intravenously (13 μl of Fenestra LC per gram of body weight of animal), and microCT scans were acquired 3 h post injection [24]. The utility of Fenestra LC in this study has been described in detail previously [25,26]. Reconstructions were performed using a cone-beam filtered back projection algorithm. The axial field of view (FOV) was set to 4.6 cm with an in-plane spatial resolution and slice thickness of 91 μm.

MRI was carried out using a 3 T MRI clinical scanner (Intera, Philips Medical System, Best, Netherlands) and a dedicated 40-mm inner diameter solenoid coil (Intera). For longitudinal monitoring of lesions, a T_2-weighted MRI technique was chosen based on previously established parameters [24]. Mice were anesthetized with isoflurane and respiratory triggered T_2-weighted images were acquired with the following parameters: FOV $8.0 \times 8.0 \times 2.0$ cm^3, data matrix 512×512, 30–40 slices, TE/TR 65/4500 ms, flip angle 90°, slice thickness 0.5 mm, 0.156×0.156 mm^2 reconstructed resolution. No contrast agent was used for MRI.

Follow-up microCT or MRI scans were conducted again at week 5 after injection of MPC cells, wherein liver lesions were approximately 3–5 mm in diameter and thus, suitable for PET scanning. Anatomical imaging was not conducted on mice receiving cells s.c., as these tumors were detected visually and measured with digital calipers. Mice with s.c. tumors were imaged with PET approximately 2 weeks after injection of MPC cells or when tumor diameter reached 3–5 mm. All nine animals with metastatic lesions were imaged using all modalities, microCT, MRI and PET. [18F]-DOPA and [18F]-DA PET was performed in the same animals for uptake comparison and in all cohorts. [18F]-DA PET was carried out within 24 h after MRI/CT imaging. [18F]-DOPA followed [18F]-DA PET imaging, also within 24 h.

2.4. Small animal PET imaging

Mice were anesthetized with isoflurane and received, via the tail vein, injection of 100 μl of 3.4 to 4.3 MBq of $[^{18}F]$-DA or 3.5–4.2 MBq of $[^{18}F]$-DOPA. PET scanning was performed using the Advanced Technology Laboratory Animal Scanner (ATLAS) PET scanner [27], which has a transverse field-of-view of 6.8 cm and an axial FOV of 2 cm. PET images were reconstructed by 2D-ordered-subset expectation maximization algorithm (five iterations and 16 subsets), achieving a 1.5 mm full width at half maximum resolution at the center [28]. The reconstructed voxel size was $0.56 \times 0.56 \times 1.125$ mm^3. No correction was applied for attenuation or scatter. Mice were positioned in the prone position on a heated animal bed near the center of FOV of the ATLAS scanner, where the highest image resolution and sensitivity was available. Dynamic data acquisitions (10 min frame duration, up to six frames) were started about 1 min after radiotracer injection and followed by whole body scans (two to three bed positions, 10 min each) immediately after the dynamic acquisition. To detect possible lung lesions, the whole body scans were set up to cover the mouse body from the salivary glands to the urinary bladder. All acquisitions were recorded with a 100–700 keV energy window.

2.5. Quantification of $[^{18}F]$-DA and $[^{18}F]$-DOPA accumulation in organ and subcutaneous pheochromocytoma lesions

To assess the $[^{18}F]$-DA and $[^{18}F]$-DOPA radiopharmaceuticals quantitatively, regions of interest (ROI) were placed over the location of the tumors and major organs (liver, kidneys, heart and muscles) in the dynamic and whole body decay-corrected images. Radiotracer uptake in samples was reported as the maximum accumulation within tumors or organs and was obtained from mean pixel values within the multiple ROIs. The results were calculated as standardized uptake values (SUVs) [29]. We also used the maximal uptake within the tumor obtained from the most active voxel cluster located within the ROI. This is equivalent to the maximum standardized uptake value (SUV_{max}) used in clinical PET studies [30].

Quantitative analyses were carried out for all identified tumors and calculated as a liver tumor-to-background ratio (TBR) and a liver tumor-to-liver ratio (TLR). TBR is equal to the SUV_{max} in tumors divided into SUV_{max} in muscle as non-target structures (background). At the end of the study, an ^{18}F-filled syringe with known activity concentration was imaged to obtain the calibration factor, expressed in MBq of ^{18}F per counts per second (CPS), for the imaging system. All ROI values, given in CPS/ml, were multiplied by this factor and divided by injected activity per mouse body weight to yield SUV values. SUV_{max} in tumors was evaluated from nine mice. The size of liver tumors was calculated from MRI as described previously [24]. Subcutaneous tumors were measured externally by calipers from week 2 onwards. At week 4, tumor size measurements were carried out. Lesions were described as 'small' if less than 5 mm in diameter and as 'big' if larger than 5 mm.

No additional efforts were undertaken for the correction of partial-volume effects and recovery. Three-dimensional ROI of tumors were determined using ATLAS software for the subsequent data analysis. The maximum standardized uptake value (SUV_{max}) was used to minimize errors due to the partial volume effect [31].

2.6. Necropsy, histopathology and catecholamine measurements

At the end of imaging, mice were sacrificed by cervical dislocation. Tumor tissues and normal organs (from control mice *n*=5) were removed and small pieces were snap frozen and stored at −80°C for catecholamine assays. The remainder was stored in 10% formalin. Tumor catecholamine levels were measured by high-pressure liquid chromatography after batch alumina extraction [32]. The presence of organ or s.c. pheochromocytoma lesions was further characterized by histopathological examination.

2.7. Immunohistochemistry

Staining was performed on formalin-fixed paraffin embedded tissue sections obtained from lesions located across multiple sites (liver, bone, ovary, adrenal glands). Sections stained for VMATs were processed according to previously described methods [33] using the primary antibodies rabbit anti-VMAT1 (1:100; Chemicon, Temecula, CA, USA) and goat anti-VMAT2 (1:500; Santa Cruz Biotechnology, Santa Cruz, CA, USA). Sections were also stained for NET using a rabbit anti-NET primary antibody (1:50; kindly provided by Dr. Christie, University of Auckland New Zealand [34]) and sheep anti-tyrosine hydroxylase (TH, 1:4000, kindly provided by Prof. P. Pilowsky, Macquarie University, Sydney Australia). For NET/TH staining, methods were identical with the exception of the blocking solution, which contained 20% donkey and 20% rat serum (Jackson Immuno, Westgrove, PA, USA) in place of 10% donkey serum. For all sections, primary antibodies were detected with species-specific secondary antibodies consisting of donkey anti-rabbit Cy3, anti-goat FITC and anti-sheep DyLight. 488 (1:500; Jackson ImmunoResearch Laboratories, West Grove, PA, USA). Negative control sections were processed concurrently according to the same methods, with omission of the primary antibody. Sections were examined using a BioRad MRC-1024 confocal microscope at excitation wavelengths of 488 and 568 nm and emission filters consisting of 522/35 and 585LP, respectively. The measurement of importance in the review of immunohistochemical slides was the presence of positive tumor cell staining. For each antibody, this was graded semiquantitatively on a five-tiered scale where 0=less than 10% of tumor cells positive; 1+=10–25% positive cells; 2+=25–50% positive cells, presented as moderate staining; 3+=50–75% positive cells, moderate to strong staining; and 4+=more than 75% of tumor cells positive, strong staining [35].

2.8. Statistical methods

Quantitative data for the in vitro and PET experiments were presented as means±S.E.M. To determine whether the two radiotracers concentrations observed in the same tumors vs. background tissues like liver and muscles differed significantly, we applied one-way analysis of variance followed by Neuman–Keuls test for group comparisons. *P*<.05 was considered to be statistically significant.

3. Results

3.1. Anatomical imaging

Hepatic contrast agent allowed microCT-based visualization of liver lesions as small as 0.35 mm in diameter, usually at the fourth week after tail vein injection of MPC cells. However,

adrenal, lung and ovarian lesions remained undetected by microCT in all animals, even at week 5 (Table 1). Liver and lung lesions were localized using T_2-weighted MRI acquisitions with respiratory triggering if larger than 0.5 mm in diameter, usually by week 4. MRI detected numerous tumors in the livers of all animals. Multiple tumors in lungs of two of the nine animals were detected by MRI and confirmed at necropsy (Table 1). Enlarged adrenal glands and ovaries larger than 2.7 mm in diameter on MRI were considered as potential tumors as it was closely described before [24]. The same adrenal gland tumors were visible by PET. However, those smaller than 2.7 mm in diameter were also confirmed with microscopic pheochromocytomas. MRI detected additional four metastases in the ovaries of four of nine mice and nine metastases in adrenal glands in five of nine mice. Necropsy confirmed the evidence of tumors at these sites (Table 1). Outcome from microCT and MRI confirmed that sizes of metastases were suitable for PET imaging at week 5 after MPC cells were injected.

3.2. Quantification of [^{18}F]-DA and [^{18}F]-DOPA accumulation in organ and subcutaneous pheochromocytoma lesions

Dynamic PET scans were recorded for up to 70 min after injection of both radiopharmaceuticals. Time–activity curves with [^{18}F]-DA (Fig. 1A) showed that the SUV_{max} for liver lesions varied depending on a tumor size. Liver tumors larger than 3 mm showed a decrease in SUV_{max} over time, while lesions smaller than 3 mm remained relatively stable. In comparison, the SUV_{max} for [^{18}F]-DOPA (Fig. 1B) in liver lesions remained stable over time regardless of tumor size. [^{18}F]-DA and [^{18}F]-DOPA uptake in liver lesions smaller than 3 mm was not significantly different from the uptake in the liver up to 50 min after their administration. Therefore, for both radiopharmaceuticals, the optimal time for lesion detection was 60–70 min after their administration, at which time TLR and SUV_{max} were the highest in both small and larger lesions, compared to liver background ($P<.001$; Fig. 1A and B). The TLR for liver lesions with [^{18}F]-DA was 1.83–2.83 depending on tumor size, whereas the TLR with [^{18}F]-DOPA was 2.26–2.71 (Table 2).

Uptake of both radiopharmaceuticals by the kidneys and liver (Table 2) was observed in both control mice and tumor bearing mice, but a significantly higher uptake was clearly apparent within metastatic lesions compared to normal unaffected tissue regions (representative coronal images shown in Fig. 2 and longitudinal images in Fig. 3). There was additional uptake apparent for [^{18}F]-DOPA in stomach wall, pancreas and spleen. Liver lesions imaged once a week for two weeks, showed a time dependent lowering of [^{18}F]-DA uptake (the first week 1.85±0.199 SUV_{max}; the second week 1.16±0.07 SUV_{max}; $P<.05$), whereas uptake of [^{18}F]-DOPA revealed similar uptake over the same time period (the first week 3.023±0.22 SUV_{max}; the second week 2.88±0.12 SUV_{max}; not significant).

Uptake of [^{18}F]-DA by s.c. tumors differed significantly from that observed in organ lesions (Fig. 3G). [^{18}F]-DA showed very low accumulation in both smaller and larger s.c. tumors (0.31±0.02 SUV_{max} for tumors <5 mm and 0.35±0.12 SUV_{max} for tumors >5 mm), almost at the level of background within muscle (0.31±0.02 $SUV_{max,}$). However, the uptake of [^{18}F]-DOPA within the same tumors was much higher [2.88±0.88 SUV_{max} for tumors <5 mm and 2.0±0.06 SUV_{max} for tumors >5 mm, ($P<.001$) than the uptake for [^{18}F]-DA

(TLR=1.56–2.24 vs. 0.22–0.27; Table 2)]. For both the organ metastatic and s.c. tumor cohorts, the uptake observed in major organs and tumors was correlated with biodistribution studies (data not presented).

Thirty to forty liver lesions were localized using [^{18}F]-DA PET in eight out of nine animals, while [^{18}F]-DOPA PET localized more than 50 liver lesions in nine animals (Table 1). Eight adrenal lesions were detected with [^{18}F]-DA in four out of nine animals compared to nine detected in five out of nine with [^{18}F]-DOPA. Four ovarian lesions were visible in four of nine animals with both radioligands, and single lung lesion was only visualized with [^{18}F]-DOPA.

3.3. Assays of [^{18}F]-DA and [^{18}F]-DOPA uptake and retention in vitro

Desipramine had a stronger inhibiting effect compared to reserpine on accumulation of [^{18}F]-DA during the initial 10-min uptake phase ($P<.05$; Fig. 4A). This indicates a strong dependence of NET for [^{18}F]-DA uptake. Desipramine decreased [^{18}F]-DA uptake to 14.3% relative to untreated cells ($P<.001$), whereas reserpine decreased [^{18}F]-DA uptake to 18.7% ($P<.001$) and tetrabenazine 20.07% ($P<.001$). The combination of desipramine and reserpine further decreased [^{18}F]-DA uptake to 2.75% ($P<.0001$). In contrast, reserpine had a stronger inhibiting effect than desipramine on the accumulation of [^{18}F]-DA after the 120 min retention phase of incubations ($P<.001$; Fig. 4B). Accumulation of [^{18}F]-DA relative to control was decreased ($P<.001$) to 40.15% after desipramine, 21.45% after reserpine, 33.83% after tetrabenazine and 25.85% after combination of desipramine and reserpine.

Relative to control cells, uptake of [^{18}F]-DOPA after the 10-min incubation period was decreased ($P<.001$) to 67.37% after desipramine, 14.03% after reserpine, 17.87% after tetrabenazine and 13.47% after the combination of desipramine and reserpine (Fig. 4C). In contrast, after the 120-min incubation period, there was no significant difference in retention of [^{18}F]-DOPA between desipramine treated and control cells (Fig. 4D). The uptake of [^{18}F]-DOPA was, however, decreased ($P<.001$) to 11.8% of control values after reserpine, to 12.1% after tetrabenazine ($P<.001$) and to 7.97% after the combination of desipramine and reserpine ($P<.001$). These results indicate strong importance of VMAT2 in accumulation and retention of [^{18}F]-DOPA in MPC cells. Statistical differences between treatments with reserpine, tetrabenazine and combination of desipramine and reserpine, compared to desipramine alone, are presented in Fig. 4.

3.4. Histopathology and immunohistochemistry: expression of monoamine transporters and tyrosine hydroxylase

Histopathology confirmed all lesions to be pheochromocytomas. Furthermore, all lesions contained high levels of catecholamines, relative to normal tissues (Table 3). The lowest ranges for expression of NE were found in s.c. lesions. All analyzed samples (2× adrenal gland lesions, 1× bone lesion, 3× liver lesions, 1× lung lesions, 1× ovarian lesion, 3 s.c. lesions) were positive for TH staining (Table 4), ranging from 2+–4+ positive staining on a five-tier scale. Ten of 11 samples showed NET staining (1+–4+). Expression of VMAT was more variable, 9 of 11 samples showing VMAT2 (2+-4+) and only 4 of 11 samples showing VMAT1 expression (1+). Furthermore, when VMAT1 was expressed (Fig. 5), it was only

present in isolated clusters of cells throughout the section, in contrast to the other markers where expression was generally more widespread in their distribution pattern. Interestingly, all s.c. lesions expressed VMAT2 but lacked expression of VMAT1. All markers were localized to the cytoplasm.

4. Discussion

The present study compared metastatic and s.c. pheochromocytoma models and established differences in the utility of PET imaging with [^{18}F]-DA and [^{18}F]-DOPA and anatomical imaging with microCT and MRI. While [^{18}F]-DA and [^{18}F]-DOPA PET performed equally well for the detection of ovarian metastatic tumors, [^{18}F]-DOPA PET showed superiority to [^{18}F]-DA PET in the detection of liver, lung and s.c. tumors. In particular, s.c. tumors were detected only with [^{18}F]-DOPA PET. Furthermore, comparisons of the in vitro uptake of both radiocompounds by MPC cells confirmed the importance of the NET for uptake of [^{18}F]-DA and also confirmed that VMAT2 and, to a lesser extent, VMAT1 is important for its retention in catecholamine storage vesicles. The VMAT2 role for the [^{18}F]-DA entry into catecholamine storage vesicles was also well demonstrated from [^{18}F]-DOPA results. It is known that [^{18}F]-DOPA is converted to [^{18}F]-DA in cytoplasm and indeed our experiments using tetrabenazine and [^{18}F]-DOPA showed the most diminished uptake of [^{18}F]-DOPA, actually [^{18}F]-DA and its storage and retention in catecholamine vesicles.

As supported by several clinical studies [36–38] functional imaging using [^{18}F]-DA and [^{18}F]-DOPA PET is a useful tool for diagnostic localization of pheochromocytomas and paragangliomas (extra-adrenal pheochromocytomas). Surgical resection of metastatic lesions is usually impossible, and biopsies are dangerous due to profound catecholamine release and a possibility of hypertensive crisis and lethal tachyarrhythmia. Our metastatic animal model provides a valuable resource for a better understanding of tumor characteristics related to experimental imaging and future targeted therapeutic interventions. We found a visibly lower accumulation of [^{18}F]-DA compared to [^{18}F]-DOPA in large liver lesions, presumably due to the decrease in the NET expression secondary to tumor dedifferentiation. [^{18}F]-DA uptake in liver lesions also decreased over longitudinal imaging, whereas for [^{18}F]-DOPA there was no decrease in the same tumors imaged over time. The differences in uptake of these two radiopharmaceuticals may be relevant to recent clinical findings of differences in functional imaging characteristics of various pheochromocytomas depending on their underlying mutations and nature [38,39]. For example, in patients with malignant paragangliomas due to succinate dehydrogenase subunit B mutations, [^{18}F]-DA is superior to [^{18}F]-DOPA for localization of metastases (reverse to the present animal model of pheochromocytoma), whereas in other patients with so called 'head-and-neck' paragangliomas, [^{18}F]-DOPA is superior to [^{18}F]-DA [37]. These tumor differences in PET imaging characteristics are suggested to reflect variations in the expression of NET, VMATs and perhaps amino acid transporter and are crucial in a current view of the choice of pheochromocytoma imaging modality.

Comparing the uptake of both radiopharmaceuticals in s.c. tumors revealed also differences. For example, s.c. tumors showed a high uptake of [^{18}F]-DOPA but no uptake of [^{18}F]-DA above the level of background. Three possibilities could explain these findings (1)

differences of blood delivery of [^{18}F]-DA and [^{18}F]-DOPA into organ metastatic and s.c. tumors; (2) the expression of cell membrane, vesicular, and amino acid transporters and their function and (3) the conversion of [^{18}F]-DOPA to [^{18}F]-DA in tumor cytoplasm and their intracellular storage or retention mechanisms. The half-life of dopamine in circulation is about 1 minute, and the half-life of ʟ-DOPA is about 40–60 min [40]. If s.c. tumors would not have enough blood supply comparing to organ metastases, taking into a consideration a different half-life of dopamine and ʟ-DOPA in plasma, this could be an important component for a lower uptake of [^{18}F]-DA to [^{18}F]-DOPA in these tumors. Another possible explanation would be the expression and function of NET. Even though the expression of NET was present in s.c. tumors and organ metastases, its function could be diminished to a greater extent in s.c. than in organ lesions. In the present animal model, the expression of NET and VMATs among excised organ and s.c. tumors was highly variable, a finding similar to previous results about NET expression in various human pheochromocytoma tissue samples based on their genetic background, location and perhaps metastatic potential [33]. Even though clusters of the NET showed different patterns of expression throughout organ and s.c. tumor samples, there was no distinct feature that could clearly explain the different [^{18}F]-DOPA and [^{18}F]-DA PET results for these lesions based on the presence of the NET. Interestingly, catecholamine measurements revealed lower values of norepinephrine (NE) in s.c. tumors comparing to organ metastases. Furthermore, VMAT1 exhibited limited expression compared to VMAT2, particularly in s.c. tumors when compared with organ metastatic lesions. In normal adrenal chromaffin and enterochromaffin cell, VMAT1 is the predominant isoform, whereas VMAT2 is typically the predominant isoform expressed in neurons of central autonomic nervous system [21,41]. This is well documented from previous studies where the uptake of [^{18}F]-DOPA in the central nervous dopaminergic system depended on the presence VMAT2 [42,43]. The present results suggest that VMAT2 is more important that VMAT1 in the accumulation of [^{18}F]-DA and [^{18}F]-DOPA (converted in cytoplasm to [^{18}F]-DA) in both organ metastatic and s.c. tumors.

There are several limitations to the present study. First, the proper function of the VMAT1 has not been investigated. Second, we did not study any presence and function of the cell membrane amino acid transporter system that is known to allow ʟ-DOPA to enter a pheochromocytoma cell; lastly, the absence of in vivo experiments manipulating (e.g., inhibiting) NET, VMAT1 and VMAT2, and amino acid transporters. However, in our preliminary experiments, the administration of desipramine, reserpine and tetrabenazine in pheochromocytoma animal model with extensive liver and other organ lesions was difficult, and side effects were in most cases fatal.

5. Conclusion

In summary, this is the first study to compare multi-imaging modalities with [^{18}F]-DOPA and [^{18}F]-DA PET, microCT and MRI for detection of organ metastatic and s.c. lesions in nude mice model of pheochromocytoma. The present data has potential relevance for explaining differences in imaging characteristics in patients with various pheochromocytomas and perhaps other neuroendocrine tumors. Subcutaneous xenografts, as in vivo tumor model, remains the most popular method for testing new imaging or treatment approaches [44]. Our data suggests that the radiotracer tumor uptake in pheochromocytomas

is different when using s.c. models, as opposed to organ metastatic models, to study the efficacy of new imaging agents.

The data should also prove useful to other studies utilizing animal models of metastatic disease in which it is desirable, if not essential, to obtain longitudinal information about the tumor development and tumor responses to treatment.

Acknowledgments

Abbreviations

PET	positron emission tomography
MPC cells	mouse pheochromocytoma cells
ROI	region of interest
FOV	field of view
TBR	tumor-to-background ratio
TLR	tumor-to-liver ratio
SUV$_{max}$	the maximum standardized uptake value
2D-OSEM	2-dimensional ordered-subsets expectation maximization
FWHM	full-width at half-maximum
[^{18}F]-DA	[^{18}F]-6-fluorodopamine
[^{18}F]-DOPA	[^{18}F]-L-6-fluoro-3,4-dihydroxyphenylalanine
VMAT1 and VMAT2	vesicular monoamine transporters 1 and 2
NET	membrane norepinephrine transporter
TH	tyrosine hydroxylase
MRI	magnetic resonance imaging
s.c.	subcutaneous
i.v.	intravenous

References

[1]. Pacak K, Koch CA, Eisenhofer G. Current approaches and new advances in endocrine hypertension. Trends Endocrinol Metab. 2002; 13:96–7. [PubMed: 11893518]

[2]. Pacak K, Eisenhofer G, Goldstein DS. Functional imaging of endocrine tumors: role of positron emission tomography. Endocr Rev. 2004; 25:568–80. [PubMed: 15294882]

[3]. Burnichon N, Rohmer V, Amar L, Herman P, Leboulleux S, Darrouzet V, Niccoli P, Gaillard D, Chabrier G, Chabolle F, Coupier I, Thieblot P, Lecomte P, Bertherat J, Wion-Barbot N, Murat A, Venisse A, Plouin PF, Jeunemaitre X, Gimenez-Roqueplo AP. The succinate dehydrogenase genetic testing in a large prospective series of patients with paragangliomas. J Clin Endocrinol Metab. 2009; 94:2817–27. [PubMed: 19454582]

[4]. John H, Ziegler WH, Hauri D, Jaeger P. Pheochromocytomas: can malignant potential be predicted? Urology. 1999; 53:679–83. [PubMed: 10197840]

[5]. Mougey AM, Adler DC. Neuroendocrine tumors: review and clinical update. Hospital Physician. 2007; 51:12–20.

[6]. Goldstein DS, Grossman E, Tamrat M, Chang PC, Eisenhofer G, Bacher J, Kirk KL, Bacharach S, Kopin IJ. Positron emission imaging of cardiac sympathetic innervation and function using 18F-6-fluorodopamine: effects of chemical sympathectomy by 6-hydroxydopamine. J Hypertens. 1991; 9:417–23. [PubMed: 1649861]

[7]. Goldstein DS, Holmes C, Stuhlmuller JE, Lenders JW, Kopin IJ. 6-[18F]fluorodopamine positron emission tomographic scanning in the assessment of cardiac sympathoneural function–studies in normal humans. Clin Auton Res. 1997; 7:17–29. [PubMed: 9074825]

[8]. Hoegerle S, Altehoefer C, Ghanem N, Koehler G, Waller CF, Scheruebl H, Moser E, Nitzsche E. Whole-body 18F dopa PET for detection of gastrointestinal carcinoid tumors. Radiology. 2001; 220:373–80. [PubMed: 11477239]

[9]. Pacak, K.; Chrousos, GP.; Koch, CA.; Lenders, JW.; Eisenhofer, G. Pheochromocytoma: progress in diagnosis, therapy, and genetics. In: Margioris, A.; Chrousos, GP., editors. Adrenal Disorders. Humana Press; Totowa: 2001. p. 479-523.

[10]. Pacak K, Eisenhofer G, Carrasquillo JA, Chen CC, Li ST, Goldstein DS. 6-[18F]fluorodopamine positron emission tomographic (PET) scanning for diagnostic localization of pheochromocytoma. Hypertension. 2001; 38:6–8. [PubMed: 11463751]

[11]. Eisenhofer G. The role of neuronal and extraneuronal plasma membrane transporters in the inactivation of peripheral catecholamines. Pharmacol Ther. 2001; 91:35–62. [PubMed: 11707293]

[12]. Arita M, Wada A, Takara H, Izumi F. Inhibition of 22Na influx by tricyclic and tetracyclic antidepressants and binding of [3H]imipramine in bovine adrenal medullary cells. J Pharmacol Exp Ther. 1987; 243:342–8. [PubMed: 2822904]

[13]. Eisenhofer G, Smolich JJ, Cox HS, Esler MD. Neuronal reuptake of norepinephrine and production of dihydroxyphenylglycol by cardiac sympathetic nerves in the anesthetized dog. Circulation. 1991; 84:1354–63. [PubMed: 1884458]

[14]. Lashford LS, Hancock JP, Kemshead JT. Meta-iodobenzylguanidine (mIBG) uptake and storage in the human neuroblastoma cell line SKN-BE(2C). Int J Cancer. 1991; 47:105–9. [PubMed: 1985865]

[15]. Havekes B, Lai EW, Corssmit EP, Romijn JA, Timmers HJ, Pacak K. Detection and treatment of pheochromocytomas and paragangliomas: current standing of MIBG scintigraphy and future role of PET imaging. Q J Nucl Med Mol Imaging. 2008; 52:419–29. [PubMed: 19088695]

[16]. Huynh TT, Pacak K, Brouwers FM, Abu-Asab MS, Worrell RA, Walther MM, Elkahloun AG, Goldstein DS, Cleary S, Eisenhofer G. Different expression of catecholamine transporters in phaeochromocytomas from patients with von Hippel-Lindau syndrome and multiple endocrine neoplasia type 2. Eur J Endocrinol. 2005; 153:551–63. [PubMed: 16189177]

[17]. Maurel A, Spreux-Varoquaux O, Amenta F, Tayebati SK, Tomassoni D, Seguelas MH, Parini A, Pizzinat N. Vesicular monoamine transporter 1 mediates dopamine secretion in rat proximal tubular cells. Am J Physiol. 2007; 292:F1592–98.

[18]. Martiniova L, Ohta S, Quion P. Anatomical and functional imaging of tumors in animal models: focus on pheochromocytoma. Ann N Y Acad Sci. 2006; 1073:392–404. [PubMed: 17102108]

[19]. Powers JF, Evinger MJ, Tsokas P, Bedri S, Alroy J, Shahsavari M, Tischler AS. Pheochromocytoma cell lines from heterozygous neurofibromatosis knockout mice. Cell Tissue Res. 2000; 302:309–20. [PubMed: 11151443]

[20]. Erickson JD, Schafer MK, Bonner TI, Eiden LE, Weihe E. Distinct pharmacological properties and distribution in neurons and endocrine cells of two isoforms of the human vesicular monoamine transporter. Proc Natl Acad Sci USA. 1996; 93:5166–71. [PubMed: 8643547]

[21]. Weihe E, Schafer MK, Erickson JD, Eiden LE. Localization of vesicular monoamine transporter isoforms (VMAT1 and VMAT2) to endocrine cells and neurons in rat. J Mol Neurosci. 1994; 5:149–64. [PubMed: 7654518]

[22]. Eisenhofer G, Hovevey-Sion D, Kopin IJ, Miletich R, Kirk KL, Finn R, Goldstein DS. Neuronal uptake and metabolism of 2- and 6-fluorodopamine: false neurotransmitters for positron emission tomographic imaging of sympathetically innervated tissues. J Pharmacol Exp Ther. 1989; 248:419–27. [PubMed: 2563292]

[23]. Weber SM, Peterson KA, Durkee B, Qi C, Longino M, Warner T, Lee FT Jr, Weichert JP. Imaging of murine liver tumor using microCT with a hepatocyte-selective contrast agent: accuracy is dependent on adequate contrast enhancement. J Surg Res. 2004; 119:41–5. [PubMed: 15126080]

[24]. Martiniova L, Kotys MS, Thomasson D, Schimel D, Lai EW, Bernardo M, Merino MJ, Powers JF, Ruzicka J, Kvetnansky R, Choyke PL, Pacak K. Noninvasive monitoring of a murine model of metastatic pheochromocytoma: a comparison of contrast-enhanced microCT and nonenhanced MRI. J Magn Reson Imaging. 2009; 29:685–91. [PubMed: 19243052]

[25]. Lee FT Jr, Chosy SG, Naidu SG, Goldfarb S, Weichert JP, Bakan DA, Kuhlman JE, Tambeaux RH, Sproat IA. CT depiction of experimental liver tumors: contrast enhancement with hepatocyte-selective iodinated triglyceride versus conventional techniques. Radiology. 1997; 203:465–70. [PubMed: 9114106]

[26]. Bakan DA, Longino MA, Weichert JP, Counsell RE. Physicochemical characterization of a synthetic lipid emulsion for hepatocyte-selective delivery of lipophilic compounds: application to polyiodinated triglycerides as contrast agents for computed tomography. J Pharm Sci. 1996; 85:908–14. [PubMed: 8877877]

[27]. Seidel J. Resolution uniformity and sensitivity of the NIH ATLAS small animal PET scanner: comparison to simulated LSO scanners without depth-of-interaction capability. IEEE Trans Nuc Sci. 2003; 50:1347–50.

[28]. Toyama H, Ichise M, Liow JS, Modell KJ, Vines DC, Esaki T, Cook M, Seidel J, Sokoloff L, Green MV, Innis RB. Absolute quantification of regional cerebral glucose utilization in mice by 18F-FDG small animal PET scanning and 2-14C-DG autoradiography. J Nucl Med. 2004; 45:1398–405. [PubMed: 15299067]

[29]. Woodard HQ, Bigler RE, Freed B. Letter: expression of tissue isotope distribution. J Nucl Med. 1975; 16:958–9. [PubMed: 1177031]

[30]. Aliaga A, Rousseau JA, Cadorette J, Croteau E, van Lier JE, Lecomte R, Benard F. A small animal positron emission tomography study of the effect of chemotherapy and hormonal therapy on the uptake of 2-deoxy-2-[F-18]fluoro-d-glucose in murine models of breast cancer. Mol Imaging Biol. 2007; 9:144–50. [PubMed: 17334852]

[31]. Keyes JW Jr. SUV: standard uptake or silly useless value? J Nucl Med. 1995; 36:1836–9. [PubMed: 7562051]

[32]. Eisenhofer G, Goldstein DS, Stull R, Keiser HR, Sunderland T, Murphy DL, Kopin IJ. Simultaneous liquid-chromatographic determination of 3,4-dihydroxyphenylglycol, catecholamines, and 3,4-dihydroxyphenylalanine in plasma, and their responses to inhibition of monoamine oxidase. Clin Chem. 1986; 32:2030–3. [PubMed: 3096593]

[33]. Cleary S, Brouwers FM, Eisenhofer G, Pacak K, Christie DL, Lipski J, McNeil AR, Phillips JK. Expression of the noradrenaline transporter and phenylethanolamine N-methyltransferase in normal human adrenal gland and phaeochromocytoma. Cell Tissue Res. 2005; 322:443–53. [PubMed: 16047163]

[34]. Kippenberger AG, Palmer DJ, Comer AM, Lipski J, Burton LD, Christie DL. Localization of the noradrenaline transporter in rat adrenal medulla and PC12 cells: evidence for its association with secretory granules in PC12 cells. J Neurochem. 1999; 73:1024–32. [PubMed: 10461891]

[35]. McDonald JW, Pilgram TK. Nuclear expression of p53, p21 and cyclin D1 is increased in bronchioloalveolar carcinoma. Histopathology. 1999; 34:439–46. [PubMed: 10231419]

[36]. King K, Chen CC, Alexopoulos DK, Whatley M, Reynolds JC, Patronas N, Ling A, Adams KT, Xekouki P, Lando H, Stratakis C, Pacak K. Functional Imaging of SDHx-Related Head and Neck Paragangliomas: comparison of 18F-fluorodihydroxyphenylalanine, 18F-fluorodopamine, 18F-fluoro-2-deoxy-d-glucose PET, 123I-metaiodobenzylguanidine scintigraphy, and 111In-pentetreotide scintigraphy. J Clin Endocr Meatb July. 2011 [epub ahead of print]. 10.1210/jc.2011-0333

[37]. Timmers HJ, Chen CC, Carrasquillo JA, Whatley M, Ling A, Havekes B, Eisenhofer G, Martiniova L, Adams KT, Pacak K. Comparison of 18F-fluoro-l-DOPA, 18F-fluoro-deoxyglucose, and 18F-fluorodopa-mine PET and 123I-MIBG scintigraphy in the localization of pheochromocytoma and paraganglioma. J Clin Endocrinol Metab. 2009; 94:4757–67. [PubMed: 19864450]

[38]. Timmers HJ, Eisenhofer G, Carrasquillo JA, Chen CC, Whatley M, Ling A, Adams KT, Pacak K. Use of 6-[18F]-fluorodopamine positron emission tomography (PET) as first-line investigation for the diagnosis and localization of non-metastatic and metastatic phaeochromocytoma (PHEO). Clin Endocrinol (Oxf). 2009; 71:11–7. [PubMed: 19138315]

[39]. Timmers HJ, Hadi M, Carrasquillo JA, Chen CC, Martiniova L, Whatley M, Ling A, Eisenhofer G, Adams KT, Pacak K. The effects of carbidopa on uptake of 6-18F-fluoro-l-DOPA in PET of pheochromocytoma and extraadrenal abdominal paraganglioma. J Nucl Med. 2007; 48:1599–606. [PubMed: 17873132]

[40]. Dutton J, Copeland LG, Playfer JR, Roberts NB. Measuring l-DOPA in plasma and urine to monitor therapy of elderly patients with Parkinson disease treated with l-DOPA and a dopa decarboxylase inhibitor. Clinical Chem. 1993; 39:629–34. [PubMed: 8472357]

[41]. Peter D, Liu Y, Sternini C, de Giorgio R, Brecha N, Edwards RH. Differential expression of two vesicular monoamine transporters. J Neurosci. 1995; 15:6179–88. [PubMed: 7666200]

[42]. Frey KA, Koeppe RA, Kilbourn MR, Vander Borght TM, Albin RL, Gilman S, Kuhl DE. Presynaptic monoaminergic vesicles in Parkinson's disease and normal aging. Ann Neurol. 1996; 40:873–84. [PubMed: 9007092]

[43]. Gilman S, Koeppe RA, Junck L, Little R, Kluin KJ, Heumann M, Martorello S, Johanns J. Decreased striatal monoaminergic terminals in multiple system atrophy detected with positron emission tomography. Ann Neurol. 1999; 45:769–77. [PubMed: 10360769]

[44]. Garber K. Realistic rodents? Debate grows over new mouse models of cancer. J Nation Cancer Institute. 2006; 98:1176–8.
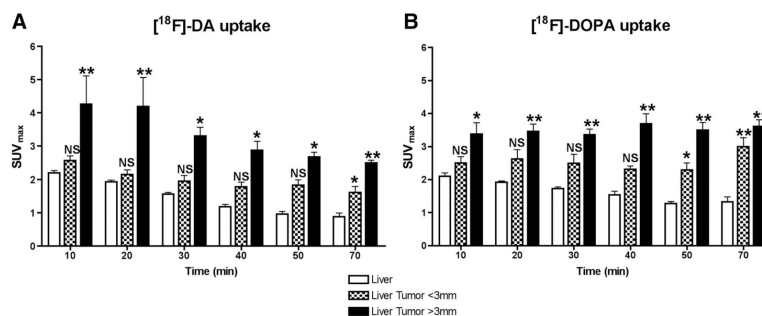
Fig. 1.
Pharmacokinetics of uptake and retention of [18F]-DA (A) and [18F]-DOPA (B) by liver tumors between 10–70 min after injection of the radiopharmaceuticals in athymic nude mice. Each bar represents mean±S.E.M. values for nine mice. From comparisons with background radioactivity in the liver, the ideal time to acquire images for quantitative analysis of liver lesions was at 60–70 min after injection of [18F]-DA and [18F]-DOPA. *P<. 05, **P<.001 versus uptake in the liver.
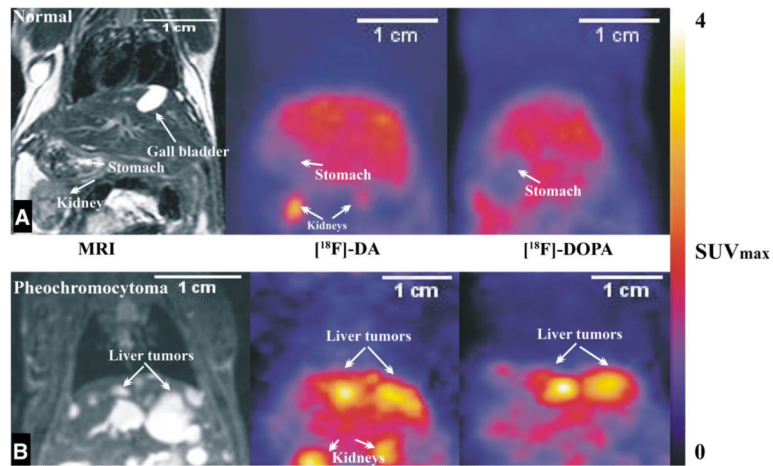
Fig. 2.
Combined coronal MRI images of representative mouse superimposed with PET images after administration of $[^{18}F]$-DA and $[^{18}F]$-DOPA to a control animal (A) and an animal previously injected with MPC cells (B). The color scale indicates maximal standardized uptake values (SUV_{max}). The usual range for liver tumors with $[^{18}F]$-DA is 1.5–2.5 SUV_{max} and for $[^{18}F]$-DOPA it is 3–3.6 SUV_{max}.
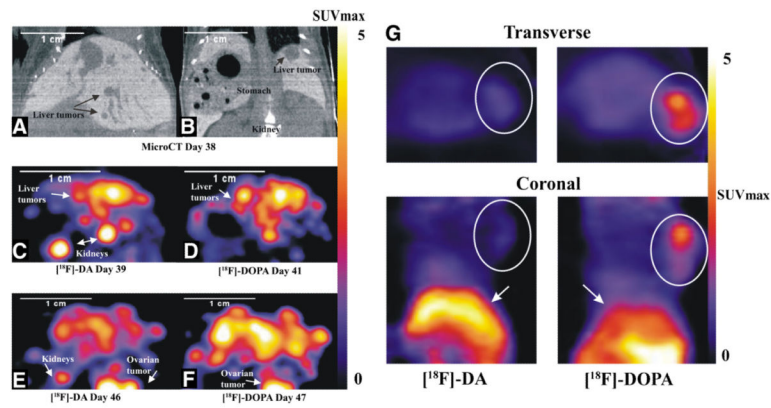
Fig. 3.

Localization of pheochromocytoma lesions by [^{18}F]-DA or [^{18}F]-DOPA PET in representative animals after i.v. (Panels 1–E) and s.c. (Panel G) injections of MPC cells. Upper panels, A and B, show microCT coronal images using Fenestra contrast agent with respiratory gating in a representative animal after i.v. injection of MPC cells. The animal was imaged on days 38 through 47 after i.v. injection of MPC cells, where panels C and E show rapid growth of liver lesions visible using [^{18}F]-DA PET over a 7-day time period. [^{18}F]-DOPA PET visualization of the same animal over consequent days is shown in panels D and F. Images were acquired at 60–70 min after injection of radiopharmaceuticals. The localization of a large s.c. tumor depicted by transverse and coronal images after s.c. injection of [^{18}F]-DA and [^{18}F]-DOPA into another representative animal is shown in Panel G. [^{18}F]-DA PET imaging reveals very low accumulation of the radiopharmaceutical in the tumor (0.35 SUV_{max}), almost at the level of nontarget tissue such as muscle (0.31 SUV_{max}). In contrast, the uptake of [^{18}F]-DOPA by the same tumor was much higher (2 SUV_{max}). Circles identify the tumor on both transverse and coronal images and arrows points to the liver.

Fig. 4.
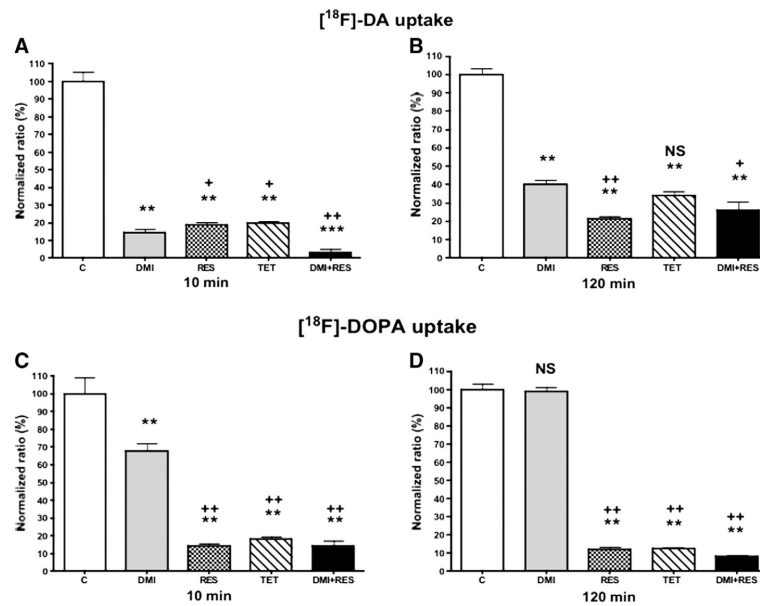Uptake of [^{18}F]-DA (A and B) and [^{18}F]-DOPA (C and D) in MPC cells presented as "normalized ratio of controls" at 10 and 120 min after treatment with 1 μM desipramine (DMI), 10 μM reserpine (RES), 10 μM tetrabenazine (TET) and their combination (30 min before adding the [^{18}F]-DA and [^{18}F]-DOPA). $*P<.05$, $**P<.001$ $***P<.0001$ versus control ("C"). $+P<.05$, $++P<.001$ versus desipramine ("DMI").
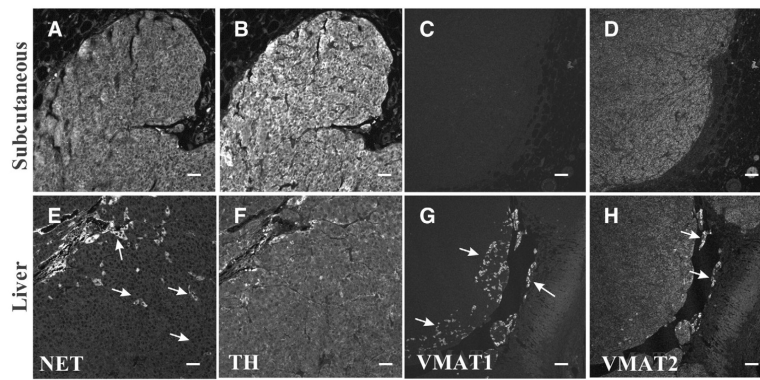
Fig. 5.
Expression profile of NET, TH and VMATs in s.c. (A–D) and liver (E–H) lesions. While the expression of TH (B, F) was consistently detected, NET (A, E) expression was variable, with strong immunoreactivity in some samples (A) but more diffuse staining with interspersed foci of strong immunoreactivity (E; arrows) in others. Typically, VMAT1 (C, G) expression was absent (C), but in some samples (G) isolated clusters of highly immunoreactive cells (arrows) were detected. Diffuse VMAT2 (D, H) staining was typically detected, including some highly immunoreactive clusters of cells (H; arrows). Bar scale: (A, B, E and F) 100 μm, (C, D, G and H) 50 μm.

Table 1

Comparison of tumors' localization by various imaging methods and confirmed with necropsy in mice injected with MPC cells

Tumors' localization

	Adrenal	Ovary	Lung	Liver	Subcutaneous
MicroCT	0	0	0	0	NA
MRI	9 in 5 mice	4 in 4 mice	>20 in 2 mice	> 50 in 9 mice	NA
[18F]-DA	8 in 4 mice	4 in 4 mice	0	30-40 in 8 mice	0
[18F]-DOPA	9 in 5 mice	4 in 4 mice	1 in 1 mouse	>50 in 9 mice	4 in 4 mice
Necropsy	18 in 9 mice	4 in 4 mice	>20 in 2 mice	>50 in 9 mice	4 in 4 mice
Mouse name	Necropsy and histopathology confirmation				
1	Multiple liver tumors (10, approx. 2–4 mm diameter); 2 enlarged adrenal glands, 2.5 mm in diameter; 1 ovarian tumor, 3 mm in diameter.				
2	Multiple liver tumors (>10, ranging from 1–5 mm diameter), 2 enlarged adrenal glands, 2.5 mm in diameter; 1 ovarian tumor, 4 mm in diameter.				
3	Single liver lesion (2.5 mm in diameter), enlarged adrenal glands, 2 mm in diameter.				
4	Multiple liver tumors (>10, ranging from 1–4 mm diameter), enlarged adrenal glands, 2 mm in diameter.				
5	Multiple liver tumors (>20, ranging from 1–3 mm diameter), 1 adrenal gland tumor, 3 mm in diameter.				
6	Multiple liver tumors (>10, ranging from 1–5 mm diameter), 2 adrenal gland tumors, 3 and 5 mm in diameter; 1 bone tumor, 5 mm in diameter; 1 lung tumor, 2 mm in diameter.				
7	Multiple liver tumors (10, ranging from 1–3 mm diameter), 1 ovarian tumor, 4 mm in diameter; 2 adrenal gland tumors, 3 mm in diameter.				
8	Multiple liver tumors (>5, ranging from 1–5 mm diameter), 2 adrenal gland tumors, 3 mm in diameter.				
9	Multiple liver tumors (>20, ranging from 1–3 mm diameter); 1 ovarian tumor; 3 mm in diameter; 2 adrenal gland tumors; 3 mm in diameter; approx. 20 lung tumors, 0.5 mm in diameter.				
All enlarged adrenal glands were confirmed as pheochromocytomas.					

MicroCT, MRI and PET imaging were performed at Week 5. All imaging modalities followed by necropsy were performed within a 24 h time window in all nine mice.

Table 2

SUV$_{max}$ in organs and tumors 60–70 min after administration of PET radioligands in mice harboring subcutaneous and organ metastatic pheochromocytomas

	[18F]-DA			[18F]-DOPA		
	SUV$_{max}$ (mean±S.E.M.)	TLR	TBR	SUV$_{max}$ (mean±S.E.M.)	TLR	TBR
Kidney	2.41±0.45	–	–	1.73±0.34	–	–
Muscle	0.31±0.02	–	–	0.29±0.02	–	–
Liver	0.88±0.11	–	–	1.33±0.14	–	–
Liver <3 mm	1.61±0.17	1.83	5.19	3.01±0.27	2.26	10.38
Liver >3 mm	2.49±0.08	2.83	8.03	3.61±0.19	2.71	12.45
Adrenal >3 mm	2.18±0.39	2.47	7.03	6.61±0.64	2.83	22.79
Ovary >3 mm	1.99±0.27	2.26	6.41	2.59±0.32	2.83	8.93
s.c. <5 mm	0.31±0.02	0.22	1.72	2.88±0.88	2.24	7.2
s.c. >5 mm	0.35±0.12	0.27	1.94	2.00±0.06	1.56	5.0

A muscle uptake was taken as a background.

Table 3

Tissue catecholamine concentrations (pg per mg of wet weight tissue) in MPC cell-derived tumors compared to concentrations in normal tissues of control female nude mice that did not receive injections of MPC cells

Catecholamines (pg/mg)			
	NE	EPI	DA
Normal values			
Liver	25–125	9–123	–
Adrenal glands	14,548–208,181	27,611–333,150	–
Ovaries	189–411	–	–
Lung	129–256	54–254	–
Tumor values			
Liver tumors	80,707–1,225,792	6496–24,716	19,532–96,128
Adrenal tumors	262,415–454,471	442,572–758,463	9325–95,300
Ovarian tumors	62,495–414,566	–	31,301–65,232
Lung tumors	95,431–4,117,381	–	29,184–1,907,137
Subcutaneous tumors	95,098–234,637	–	37,314–54,085

Catecholamine concentrations are shown as ranges of values. EPI, epinephrine; DA, dopamine.

Table 4

Expression of TH, NET, and VMATs in tumor samples (0=less than 10% of tumor cells positive; 1+=10–25% positive cells; 2+=25–50% positive cells, presented as moderate staining; 3+=50–75% positive cells, moderate to strong staining; and 4+=more than 75% of tumor cells positive, strong staining)

Location	TH	NET	VMAT1	VMAT2	[18F]-DA	[18F]-DOPA (SUV_max)
Adrenal 1	4+	2+	1+	4+	2.15	6.46
Adrenal 2	4+	3+	1+	3+	1.98	5.79
Bone	4+	2+	0	0	—	1.42
Liver 1	3+	1+	0	3+	2.46	3.31
Liver 2	4+	3+	1+	4+	1.89	2.79
Liver 3	2+	0	0	0	—	3.24
Lung	2+	4+	0	3+	—	1.15
Ovary	4+	2+	1+	2+	1.92	3.05
s.c. 1	4+	2+	0	2+	—	1.88
s.c. 2	3+	3+	0	3+	—	2.25
s.c. 3	4+	4+	0	2+	—	2.09

[18F]-DA and [18F]-DOPA PET uptake in organ metastatic and s.c. tumors expressed in SUV_max; calculated from images after 60–70 min after administration. Numbers 1–3 indicate number of samples. A dash sign "—" presents SUV_max values less than 0.3 for both [18F]-DA and [18F]-DOPA.